

A (full) waveform inversion based on pure P- and S- wave separation

Hassan Khaniani, Shahpoor Moradi and Daniel Trad

ABSTRACT

The use of fully elastic wave equation in seismic Reverse Time Migration (RTM) and Full Waveform Inversion (FWI) has the artifact of collocation of P- and S- wave. We show that collocation of the P- and S- waves produce crosstalk errors which produce uncertainty in migration and FWI result. We develop a waveform migration and inversion algorithm using separation of P- and S- wave and the gradient function of FWI. A multicomponent RTM is developed that is based on the propagation of pure P- and S- wave. With the multicomponent forward propagation of sources and the backward propagation of receivers, we apply the formulation of FWI for multiparameter extraction with less uncertainty as compared to the use of the full elastic propagation.

INTRODUCTION

In exploration seismology, the method of iterative waveform inversion has led to significant advances subsurface parameter estimation. The method is also referred to as Full Waveform Inversion (FWI) that is an optimization problem based on perturbation theory, where the perturbations in model parameters are related to the perturbation in data (Taran-tola, 1984). The perturbation in data is referred with different terminologies such as scattered wave, data residual and reflectivity function (Beylkin, 1985; Bleistein, 1979). The FWI method is well received in geoscience studies predominantly because of its iterative optimization algorithm. An initial model close to the true model is chosen to migrate the data residual and estimate the gradient function. The algorithm requires a properly scaled gradient function (which is sensitive to model parameters) to update the initial model and the process is iterated until the data residual is small enough. For solution of the optimization problem, the main steps in an FWI algorithm are forward modeling, migration, and inversion.

The goal of FWI is to include all information contained in waveforms such as traveltimes, amplitudes, phase and their combinations in inversion. The limitations in acquisition parameters and processing steps cause to limit the use of waveform information in FWI. In practice, having proper acquisition parameters such as spatial and temporal sampling, source and receivers configuration is difficult in complex structures. In addition, obtaining the initial model close to the true model is a huge part of inversion which often is ignored by researchers. Sometimes a smoothed version of the true model is considered as an initial model which is a simplification of the inverse problem, see e.g., (Schuster, 2015).

Forward modeling and migration/inversion are the main steps in FWI. Although the forward modeling can predict all types of reflected waves such as primaries and multiples, but the main concern for inversion is from the limitation of migration algorithms to properly handle the events. Migration operators are often based on the primary wavefield and cannot sufficiently handle true amplitude imaging of multiples. The recorded data in an elastic medium contain primaries and several orders of P- and S-waves multiples. In an elastic seismogram, due to the linearization of RTM and the simultaneous backpropagation

of data (P- and S-waves) produce an image of P- and S waves that may be overlapped in space (Chang and McMechan, 1994) and have a destructive interface. Sun and McMechan (Sun and McMechan, 1994) show that the given input model for RTM can influence the polarity of P- and S-wave in the migration result. If reflected P- and S-waves can be separated and migrated independently with their respective velocities, we can not only avoid the destructive interference between polarity-reversed energy but also obtain independent P- and S-images. Alternatively, images produced by extrapolation with an elastic wave equation during migration may be separated concurrently with the application of the imaging condition. P-S wave separation was initiated by Dankbaar (1985). Dellinger and Etgen (1990) presented anisotropic P-S wave separation in propagating elastic waves using divergence-like and curl-like operators to project the full wavefield displacement in direction of polarization vectors of desired wave modes. The curl and divergence operators reduce the artifacts of P- and S- wave collocation in full-wave equation RTM.

Recently a Finite Difference Time Domain (FDTD) modeling for isotropic elastic wave with separation of pure P- and S- modes are developed by Chen (2014). In this study, we use similar decoupled system of first order wave equation to modify the migration and gradient function in FWI. The decoupled system of elastic wave equations have the advantage of less computation time compared to full-wave equation. The approach is different from previous studies as we obtain the inversion from the waveform information of two separate images of pure P-P and P-to-S-waves. In this direction, we developed a multicomponent RTM and inversion algorithm that the source forward propagation and receiver backward propagation are solved with pure P- and S-waves. The advantage of the method is that the waveform of the seismogram is preserved after imaging. In P-P migration, the waveforms of P-wave are preserved by dilatation operators of acoustic wave equation but the curl forms of S-waves are distorted. Similarly, applying pure S- wave equation for backward extrapolation of data preserve the waveforms of S-wave, while it distorts the compressional waves. With numerical examples, we show that separation of the P- and S-waves reduce the uncertainty of inversion. The approach is applicable to all primary reflected conserved and converted modes such as P-to-P, S-to-S, P-to-S, S-to-P. For this study, we demonstrate the application of the method on P-to-P and P-to-S waves. For the P-to-P scenario, the P-wave source forward propagation and the receiver backward propagation are solved with pure P-wave (acoustic) approximation. For the P-to-S wave imaging, the propagation of forwarding source is solved with pure P- wave approximation while the receiver backward propagation is solved with the pure S-wave equation. Because of the multicomponent output of RTM, its imaging condition is based on the FWI formula of (Tarantola, 1986, 1988), where the bulk modulus is inverted by the P-to-P wave while the shear modulus is inverted by P-to-S wave imaging.

WAVEFORM INVERSION

In wave equation, the displacement vector $\mathbf{u}(\mathbf{x}, t)$ and stress σ satisfies in the following equation

$$\rho(\mathbf{x}) \frac{\partial^2 u^i}{\partial t^2}(\mathbf{x}, t) - \frac{\partial \sigma^{ij}}{\partial x^j}(\mathbf{x}, t) = 0, \quad (1)$$

We use the single scattering approximation called Born approximation to the wave

equation (1). The perturbations in density ρ , stiffness tensor c_{ijkl} , strain tensor ϵ and displacement \mathbf{u} are given by

$$\begin{aligned}\rho(\mathbf{x}) &\longrightarrow \rho(\mathbf{x}) + \delta\rho(\mathbf{x}), \\ c^{ijkl}(\mathbf{x}, t) &\longrightarrow c^{ijkl}(\mathbf{x}, t) + \delta c^{ijkl}(\mathbf{x}, t), \\ \epsilon^{kl}(\mathbf{x}, t) &\longrightarrow \epsilon^{kl}(\mathbf{x}, t) + \delta\epsilon^{kl}(\mathbf{x}, t), \\ u^i(\mathbf{x}, t) &\longrightarrow u^i(\mathbf{x}, t) + \delta u^i(\mathbf{x}, t),\end{aligned}\tag{2}$$

where, $\epsilon^{kl}(\mathbf{x}, t)$ is the strain tensor. Inserting (2) in equations (1)

$$(\rho(\mathbf{x}) + \delta\rho(\mathbf{x})) \frac{\partial^2(u^i + \delta u^i)}{\partial t^2}(\mathbf{x}, t) - \frac{\partial(\sigma^{ij} + \delta\sigma^{ij})}{\partial x^j}(\mathbf{x}, t) = 0,\tag{3}$$

where perturbation in stress $\sigma^{ij}(\mathbf{x}, t) + \delta\sigma^{ij}(\mathbf{x}, t)$ is defined by,

$$\sigma^{ij}(\mathbf{x}, t) + \delta\sigma^{ij}(\mathbf{x}, t) = \{c^{ijkl}(\mathbf{x}) + \delta c^{ijkl}(\mathbf{x})\} \{\epsilon^{kl}(\mathbf{x}, t) + \delta\epsilon^{kl}(\mathbf{x}, t)\}.\tag{4}$$

Keeping the first order of perturbations we arrive at the following inhomogeneous equations with new sources

$$\rho(\mathbf{x}) \frac{\partial^2 \delta u^i}{\partial t^2}(\mathbf{x}, t) - \frac{\partial \delta \sigma^{ij}}{\partial x^j}(\mathbf{x}, t) = -\delta\rho(\mathbf{x}) \frac{\partial^2 u^i}{\partial t^2}(\mathbf{x}, t).\tag{5}$$

So the right hand side of equation (5) represents the density force term. Now, using the integral solution of the wave equation and given the new source terms, scattered wave δu^i is given by

$$\begin{aligned}\delta u^i(\mathbf{x}, t) &= \\ &- \int_V d\mathbf{x}' \int_{t_0}^{t_1} dt' G^{ij}(\mathbf{x}, t; \mathbf{x}', t') \delta\rho(\mathbf{x}') \frac{\partial \delta u^j}{\partial t^2}(\mathbf{x}', t') \\ &- \int_V d\mathbf{x}' \int_{t_0}^{t_1} dt' \frac{\partial G^{ij}}{\partial x'^k}(\mathbf{x}, t; \mathbf{x}', t') \delta c^{ijklm}(\mathbf{x}') \epsilon^{lm}(\mathbf{x}', t').\end{aligned}\tag{6}$$

In this equation, the retarded or causal Green's tensor $G^{ij}(\mathbf{x}, t; \mathbf{x}', t')$ propagates the wave forward in time from $(\mathbf{x}', t') < (\mathbf{x}, t)$ to (\mathbf{x}, t) . For an isotropic medium the model parameter \mathbf{m} can be defined by the spatial distributions of the P wave velocity, $V_P(\mathbf{x})$, the S- wave velocity, $V_S(\mathbf{x})$, and density, $\rho(\mathbf{x})$ that is

$$\mathbf{m}(\mathbf{x}) = [V_P(\mathbf{x}), V_S(\mathbf{x}), \rho(\mathbf{x})].$$

Considering the perturbation in the displacement in terms of perturbations in the model parameters we have

$$\begin{aligned}\delta \mathbf{u} &= \int_V d\mathbf{x}' \frac{\partial \mathbf{u}}{\partial \mathbf{m}} \delta \mathbf{m} = \\ &\int_V d\mathbf{x}' \left\{ \frac{\partial \mathbf{u}}{\partial \rho} \delta \rho + \frac{\partial \mathbf{u}}{\partial \kappa} \delta \kappa + \frac{\partial \mathbf{u}}{\partial \mu} \delta \mu \right\},\end{aligned}\tag{7}$$

where, the Fréchet kernels are given by

$$\begin{aligned}
\frac{\partial u_i}{\partial \rho} &= - \int_{t_0}^{t_1} dt' G^{ij}(\mathbf{x}, t; \mathbf{x}', t') \frac{\partial u^j}{\partial t^2}(\mathbf{x}', t'), \\
\frac{\partial u_i}{\partial \kappa} &= - \int_{t_0}^{t_1} dt' \frac{\partial G^{ij}}{\partial x'^k}(\mathbf{x}, t; \mathbf{x}', t') \delta^{jk} \delta^{lm} \varepsilon^{lm}(\mathbf{x}', t'), \\
\frac{\partial u_i}{\partial \mu} &= - \int_{t_0}^{t_1} dt' \frac{\partial G^{ij}}{\partial x'^k}(\mathbf{x}, t; \mathbf{x}', t') \left(\delta^{jl} \delta^{km} + \delta^{jm} \delta^{kl} - \frac{2}{3} \delta^{jk} \delta^{lm} \right) \varepsilon^{lm}(\mathbf{x}', t').,
\end{aligned} \tag{8}$$

To invert the properties we calculate the adjoint of equation (7)

$$\delta \hat{\mathbf{m}}(\mathbf{x}') = \int d\mathbf{x} \int dt \left[\frac{\partial \mathbf{u}}{\partial \mathbf{m}}(\mathbf{x}, t; \mathbf{x}') \right]^* \delta \mathbf{u}(\mathbf{x}, t), \tag{9}$$

In the above equations the Green's function is the advanced Green's function, which is anti-causal propagator. In other words, it propagates the wavefield backward in time. As a result, the backscattered wave in time is defined as

$$\delta u_j(\mathbf{x}', t') = \int d\mathbf{x} \int dt G^{ij}(\mathbf{x}', t'; \mathbf{x}, t) \delta u_i(\mathbf{x}, t), \tag{10}$$

where the advanced Green's function $G^{ij}(\mathbf{x}', t'; \mathbf{x}, t)$ propagate the residual wave $\delta u_i(\mathbf{x}, t)$ back in time from $(\mathbf{x}, t) > (\mathbf{x}', t')$ to (\mathbf{x}', t') . The inversion formula can be written in terms of forwarded wavefield $\mathbf{u} = \mathbf{U}^F$ and backward waves $\delta \mathbf{u} = \mathbf{U}^B$,

$$\begin{aligned}
\text{(a)} : \delta \hat{\rho}(\mathbf{x}) &= - \int dt \frac{\partial U_j^F}{\partial t} \frac{\partial U_j^B}{\partial t}, \\
\text{(b)} : \delta \hat{\kappa}(\mathbf{x}') &= - \int dt \sum_l \frac{\partial U_l^F}{\partial x^l} \sum_k \frac{\partial U_k^B}{\partial x^k}, \\
\text{(c)} : \delta \hat{\mu}(\mathbf{x}') &= - \int dt \sum_{lm} \left(\frac{\partial U_l^F}{\partial x^m} + \frac{\partial U_m^F}{\partial x^l} \right) \left(\frac{\partial U_l^B}{\partial x^m} + \frac{\partial U_m^B}{\partial x^l} \right) - \frac{2}{3} \int dt \sum_l \frac{\partial U_l^F}{\partial x^l} \sum_k \frac{\partial U_k^B}{\partial x^k}.
\end{aligned} \tag{11}$$

The forward problem of the 2D elastodynamic wave equation (1) in isotropic media is sometimes expressed as a coupled system of first-order differential equations, which are used for the solution of the particle velocities and stresses (Virieux, 1986). Figure (1) shows a schematic of three phases of a particle motion in the wave equation that are considered in inversion formula (11). The translation phase describes the acceleration of particles which is related to the medium density. The dilatation phase describes the change in volume of the particles, which is related to bulk modulus. The shearing strain occurs as a result of shear stress, which is related to the shear modulus.

The inverse problem in equation (11) is based on correlation of parameters of forward source \mathbf{U}^F and backward receiver wavefields $\delta \mathbf{u} = \mathbf{U}^B$. The formula implies RTM imaging condition based on translation, dilatation and shearing strategies, where the density in equation (11a) is extracted by correlation of the time derivatives of forwarding source and backward receivers, which describes the acceleration of the translated particle. The bulk

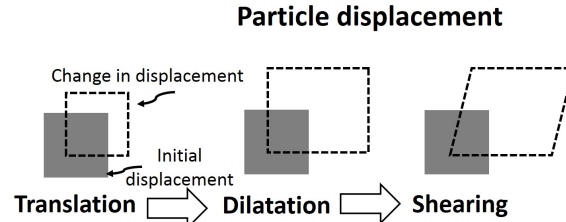


FIG. 1. Elastic model scatter point and the schematic of the contribution of translation, dilatation and shearing in the wave propagation. In the inversion formulation the density is extracted based on acceleration of translation, the bulk modulus is related to the dilatation of P-wave and shearing modulus is related to shearing stress of S-wave.

modulus in equation (11b) is proportional to the correlation of divergence of forwarding source and backward receiver wavefield referred as the dilatation quantity. Main contribution of the shear modulus estimation in equation (11c) is from the correlation of shear stress of forward source and backward receivers, as the contribution of last term in equation (11c) is negligible for the backward propagated S-wave.

Efficiency of the inversion formula

The maximum amplitude of the inversion formulation (11) occurs at the scatterpoint position, where the correlation of forwarding source and backward propagated receiver field is maximum. Figure (2) shows schematic of the response of four scatterpoints to an incident P-wave in an isotropic medium. As shown in Figure (2a) the polarization of propagated P-wave toward receivers are depicted. Each scatterpoint is described by the contrast in elastic properties, e.g., V_P and V_S . The sign "+" represents a positive contrast. According to Huygens principle, the superposition of all scatterpoint responses at a reflection boundary generates the reflector. The scattered polarization vectors have canceling effects on each other, while only the polarization vectors at specular points add constructively. For a P-wave the polarization vector is parallel to the slowness of propagation). In Figure (2a), the schematics of the polarization vectors at the reflection boundary are plotted based on AVO effects and the direction of the reflected wave. Their patterns are symmetric with respect to the x and z-axis originated from the source position. In Figure (2b) the schematics of the rotation of a scattered P-to-S wave at a reflection specular point is depicted, where these rotations are symmetric with respect to the x and z-axis originated from the source position. An AVO effect on the polarization of scattered S-wave (i.e., perpendicular to the direction of propagation) is applied on the reflection point. As seen, they have a negative sign of rotation and polarization which should be accounted for imaging/inversion problems. In next section, we describe the development of an algorithm that corrects all the polarity reversals for imaging.

Comparison of the polarization vectors in Figures (2a and b) shows that they have crosstalk on the result of inversion. In the next section, we use a numerical experiment to show that for a P-to-P wave the result of the first term in equation (11) increases with offsets, which creates an artifact in inversion results if collocated with the S-wave. Similarly the P-to-S wave, the contribution of $\nabla \cdot \mathbf{U}$ increases with offset, which creates errors to the result of inversion from collocated P-wave.

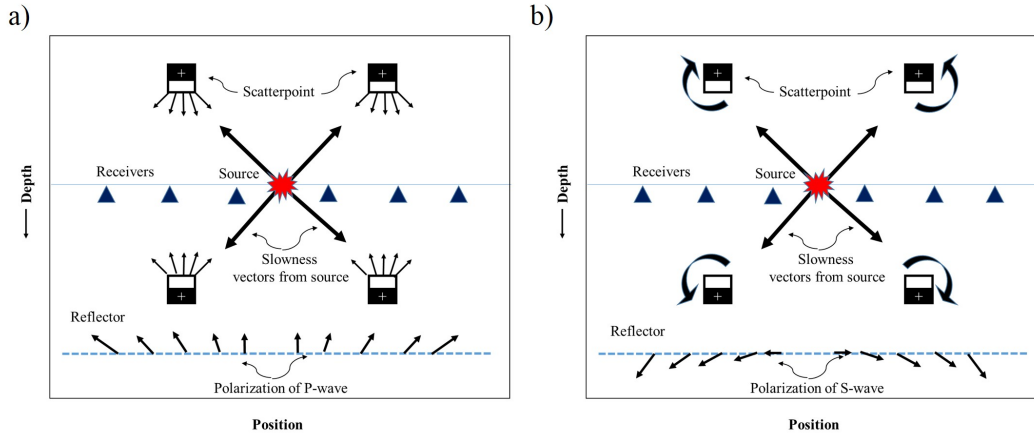


FIG. 2. Polarization patterns of a) P-to-P and b) P-to-S waves. The response of four scatterpoints toward the receivers are schematically plotted on the scatterpoint and reflector boundaries. The arrows in reflection boundaries are the polarization of reflected P- and S- wave which has the main contribution in FWI formulations.

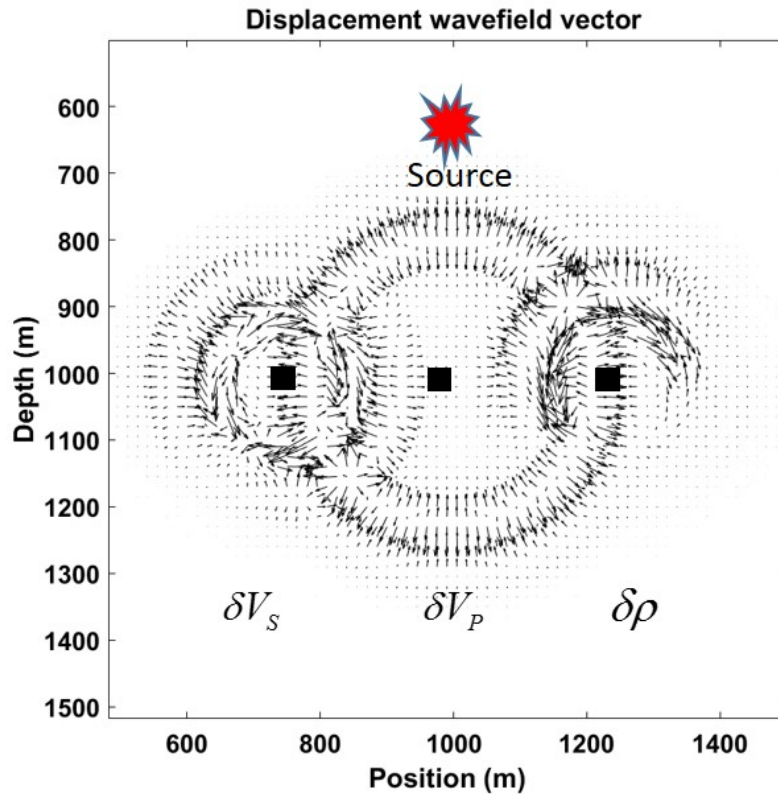


FIG. 3. Numerical illustration of sensitivity of model parameters. The arrows show the displacement field of the wavefield at $t=0.2$ s. The background color represent the inversion parameters which are related to b) dilatation and c) rotation. The arrows are normalized for representation.

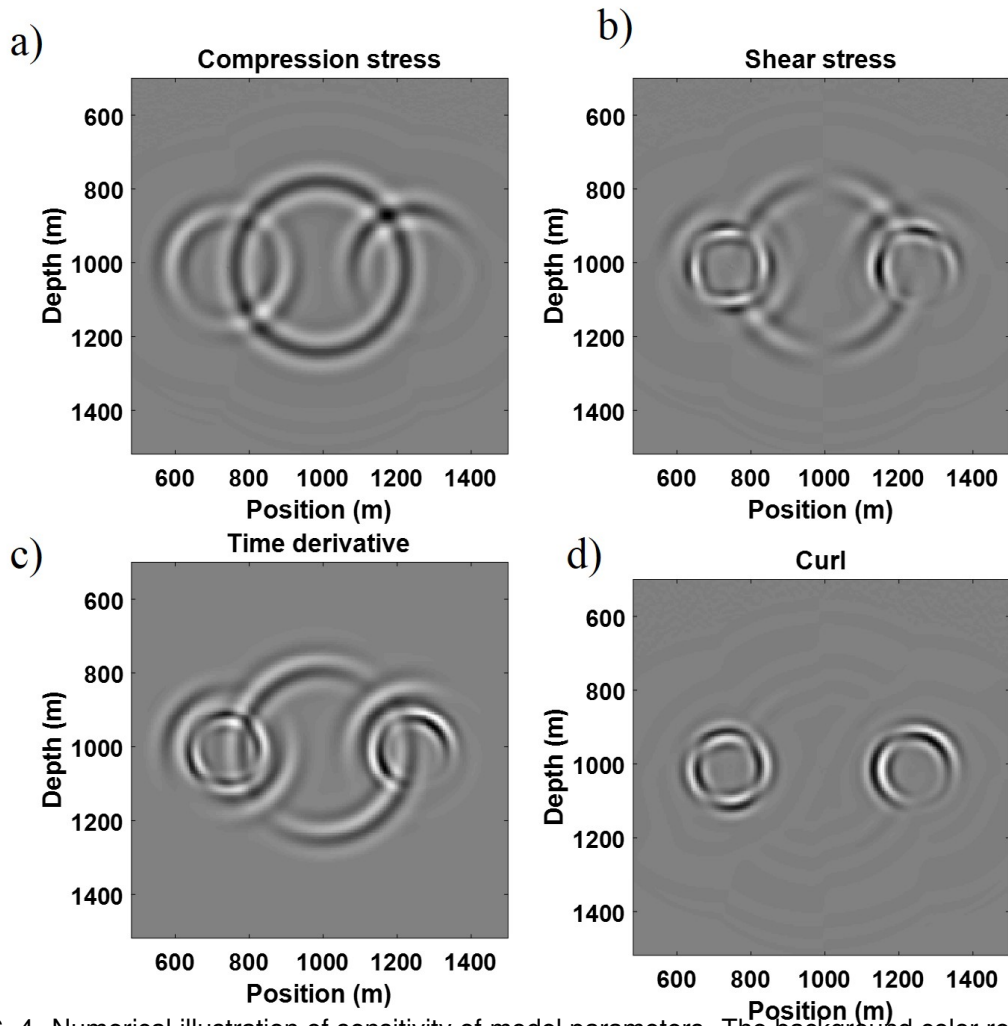


FIG. 4. Numerical illustration of sensitivity of model parameters. The background color represents a) compression stress, b) shear stress, c) time derivative and d) curl of the wavefield.

In equation 11 the variables can be expressed in terms of different model parameters. An infinitesimal changes in new parameters \mathbf{M} in terms of old parameters \mathbf{m} can be written as

$$\delta\hat{\mathbf{M}}(\mathbf{x}) = \int dt' \left[\frac{\partial \mathbf{u}(\mathbf{x}, t')}{\partial \mathbf{m}(\mathbf{x})} \frac{\partial \mathbf{m}(\mathbf{x})}{\partial \mathbf{M}(\mathbf{x})} \right]^* \delta \mathbf{u}(\mathbf{x}, t') = \frac{\partial \mathbf{m}(\mathbf{x})}{\partial \mathbf{M}(\mathbf{x})} \int dt' \left[\frac{\partial \mathbf{u}(\mathbf{x}, t')}{\partial \mathbf{m}(\mathbf{x})} \right]^* \delta \mathbf{u}(\mathbf{x}, t').$$

We can simplify the above equation using relation (7) and write

$$\delta\hat{\mathbf{M}}(\mathbf{x}) = \frac{\partial \mathbf{m}(\mathbf{x})}{\partial \mathbf{M}(\mathbf{x})} \delta \hat{\mathbf{m}}(\mathbf{x})$$

Assuming that $\mathbf{m} = (\rho, \kappa, \mu)$ and $\mathbf{M} = (\rho, V_P, V_S)$ we can write

$$\begin{aligned} \delta\hat{\rho} &= \frac{\partial \kappa}{\partial \rho} \delta\hat{\kappa} + \frac{\partial \mu}{\partial \rho} \delta\hat{\mu} + \frac{\partial \rho}{\partial \rho} \delta\hat{\rho}, \\ \delta\hat{V}_P &= \frac{\partial \kappa}{\partial V_P} \delta\hat{\kappa} + \frac{\partial \mu}{\partial V_P} \delta\hat{\mu} + \frac{\partial \rho}{\partial V_P} \delta\hat{\rho}, \\ \delta\hat{V}_S &= \frac{\partial \kappa}{\partial V_S} \delta\hat{\kappa} + \frac{\partial \mu}{\partial V_S} \delta\hat{\mu} + \frac{\partial \rho}{\partial V_S} \delta\hat{\rho}, \end{aligned} \quad (12)$$

where, the relationship between the velocities and bulk and shear modulus are given by

$$V_P = \sqrt{\frac{\kappa + \frac{4}{3}\mu}{\rho}}, \quad \text{or} \quad \kappa = \rho V_P^2 - \frac{4}{3}\rho V_S^2, \quad (13)$$

$$V_S = \sqrt{\frac{\mu}{\rho}}, \quad \text{or} \quad \mu = \rho V_S^2. \quad (14)$$

Other model parametrization are also available (see e.g., $\mathbf{M} = (\rho, \lambda, \mu)$, $\mathbf{M} = (Z_P, Z_S)$). The radiation patterns of the scattered waveform with respect to these model parameters are illustrated by Tarantola (1986). These patterns are derived based on analytical angle-dependent reflectivity functions (Aki and Richards, 2002) or scattering potentials of Born approximation. In this study, we perform the numerical examples based on the perturbation in $V_P(\mathbf{x})$, $V_S(\mathbf{x})$ and $\rho(\mathbf{x})$, but the inversion formula of equation 11 are performed for extraction of $\mathbf{m} = (\rho, \kappa, \mu)$.

The scattering potential formulations of isotropic medium show that the amplitude of the conserved mode P-to-P wave is sensitive to the perturbation in $V_P(\mathbf{x})$, $V_S(\mathbf{x})$ and $\rho(\mathbf{x})$, but the amplitude of the S-to-S and mode converted P-to-S wave is only sensitive to $V_S(\mathbf{x})$ and $\rho(\mathbf{x})$ parameters (see e.g., Beylkin and Burridge (1990)). In Figure (3), we use a numerical example for illustration of the sensitivities of these three parameters to the incident P-wave. A 2D model with three scatter points is considered with 10 perturbation of background models $V_P(\mathbf{x})$, $V_S(\mathbf{x})$ and $\rho(\mathbf{x})$. The simulation is performed by FDTD of elastic wave with background model of $V_P(\mathbf{x}) = 2000$ m/s, $V_S(\mathbf{x}) = 1250$ m/s, and $\rho(\mathbf{x}) = 2000$ kg/m³ with grid size of $Dx=5$ m, Ricker wavelet with dominant frequency of 30 Hz and time stepping of $Dt=1.2$ ms. In Figure (4), different properties are extracted from the wavefield in Figure (3). The background color in (3)a corresponds to the compressional

stress, which in an isotropic medium is proportional to the $\nabla \cdot \mathbf{U}$ of the scattered P-wave. As seen in Figure (4b), both of P-to-P and P-to-S waveform contain the shear stress, but the shear stress is stronger in P-to-S waves. For illustration, in (4d) the shear wave is isolated from the P-wave by applying curl on the wavefield, as the displacement is perpendicular to the wavefront. In (4 c), the density is extracted based on time derivative of the wavefield as expressed in equation (11). As seen due to dilatation properties of P-wave, without the consideration of radiation patterns, the separation of model parameters $V_P(\mathbf{x})$, $V_S(\mathbf{x})$ and $\rho(\mathbf{x})$ are not efficient if equation (11) is used for P-to-P wavefield. Similarly, separation of $V_S(\mathbf{x})$ and $\rho(\mathbf{x})$ is difficult without considering the radiation pattern of the scatterpoints. Furthermore, the use of time derivatives alone can not separate P- and S- waves and in our experiment is not an efficient approach to distinguish the density variations from other parameters.

WAVEFORM INVERSION USING P-AND S-WAVE SEPARATION

The inversion formulation in equation (11) is a multicomponent migration with specific imaging conditions that are designed for inversion. A typical full wave equation migration algorithm collocates the images of P- and S-waveforms. The image output of P- and S-waves have different polarity and amplitude which eventually lead to distorting the quality of migration image. In the context of inversion, we show that a similar strategy for migration lead to inaccuracy of the inversion result.

The reflected wavefields from the contrast in $V_P(\mathbf{x})$ and $V_S(\mathbf{x})$ are compared in Figure (4b). Both parameters affect the results of inversion from each other. For the contrast in $V_P(\mathbf{x})$, the inversion result is proportional to the compressional stress σ_{ii} . As, seen in b, the shear stress is not negligible and affects the result of inversion for μ . As seen in Figure (4c), the contrast in $V_S(\mathbf{x})$ create reflected P-wave that has compressional stress. The shear stress σ_{12} due to $V_S(\mathbf{x})$ in Figure (4d) shows that on the collocation of P- and S- waves, extraction of multiparameters are involved with errors that come from the superposition of different types of wavefield for reconstruction of the migration image.

Algorithm description

In this section, we developed an algorithm for multicomponent migration to reduce the uncertainty of model parameter inversion in equation (11). For a 2D case, the propagation of P-wave is solved with first-order wave equation,

$$\begin{aligned}
 \frac{\partial v_1}{\partial t} &= V_P^2 \frac{\partial \mathcal{D}}{\partial x_1}, \\
 \frac{\partial v_2}{\partial t} &= V_P^2 \frac{\partial \mathcal{D}}{\partial x_2}, \\
 \frac{\partial v_3}{\partial t} &= V_P^2 \frac{\partial \mathcal{D}}{\partial x_3}, \\
 \frac{\partial \mathcal{D}}{\partial t} &= \frac{\partial v_1}{\partial x_1} + \frac{\partial v_2}{\partial x_2} + \frac{\partial v_3}{\partial x_3},
 \end{aligned} \tag{15}$$

where, the term \mathbf{v} is the particle velocity, \mathcal{D} is the pressure defined as $\mathcal{D} = \nabla \cdot \mathbf{U}$. For the S-wave propagation we used the following system of equation,

$$\begin{aligned}
 \frac{\partial v_1}{\partial t} &= -V_S^2 \left(\frac{\partial C}{\partial x_2} + \frac{\partial B}{\partial x_3} \right), \\
 \frac{\partial v_2}{\partial t} &= V_S^2 \left(\frac{\partial C}{\partial x_1} - \frac{\partial A}{\partial x_3} \right), \\
 \frac{\partial v_3}{\partial t} &= V_S^2 \left(\frac{\partial A}{\partial x_2} + \frac{\partial B}{\partial x_1} \right), \\
 \frac{\partial A}{\partial t} &= \frac{\partial v_2}{\partial x_3} - \frac{\partial v_3}{\partial x_2}, \\
 \frac{\partial B}{\partial t} &= \frac{\partial v_1}{\partial x_3} - \frac{\partial v_3}{\partial x_1}, \\
 \frac{\partial C}{\partial t} &= \frac{\partial v_1}{\partial x_2} - \frac{\partial v_2}{\partial x_1},
 \end{aligned} \tag{16}$$

where, the terms A, B and C are the components of rotational field (i.e., $(A, B, C) = \nabla \times \mathbf{U}$). For a 2D study, the terms A and C disappear in equation (16). The numerical evaluations for S-wave forward propagation in a 2D problem are performed by Chen (2014). Figure (5) shows the algorithm that we developed for the migration and inversion of multi-component data based on wave separation. For migration, the wavefield of source forward propagation particle velocity \mathbf{U}^F and compressional stress \mathcal{D}^F are solved by equation (15). The receiver backward propagation for P-to-P migration is solved by time reversal of equation (15) where, backward propagation of particle velocity \mathbf{U}^B and compressional stress \mathcal{D}^B are estimated and stored at each time step. The receiver backward propagation for P-to-S migration is solved by time reversal of equation (16), where backward propagation of particle velocity \mathbf{U}^B and curl components A, B and C are estimated and stored at each time step. The numerical solution scheme is based on the FDTD of staggered grid in a leapfrog scheme with the Unsplit Perfectly Matched Layers (USPML) boundary condition of Zhou (2005).

The multicomponent extrapolation of displacement vector field in the medium, facilitates application of equation (11) on inversion of parameters for separated wavefield. The gradient function $\delta \hat{\kappa}(\mathbf{x}')$ is obtained by correlation of compressional stress \mathcal{D}^F and \mathcal{D}^B of P-to-P RTM are applied, while for inversion of $\delta \hat{\mu}(\mathbf{x}')$ correlation of shear stress the first term of P-to-S RTM has the main contribution to inversion result. The perturbation of density create both compressional and shear waves. In our experience, the uncertainty of density extraction without consideration of radiation patterns of density is a high and is skipped in this study.

A synthetic numerical model was created from a two-layer model as shown in Figure (6). The elastic FDTD forward modeling is used to produce a single shot record, with a maximum of 1000 m offset with a receiver spacing of $Dx=2$ m. For illustration purposes, an explosive source is positioned in depth of 700 m below the surface. This helps to have primary P-to-P and P-to-S data and avoid the interference of other types of waves such as S-to-S, S-to-P and their multiple reflections with them. A zero phase wavelet with a dominant frequency of 35 Hz was arbitrarily chosen. The migration results are shown in

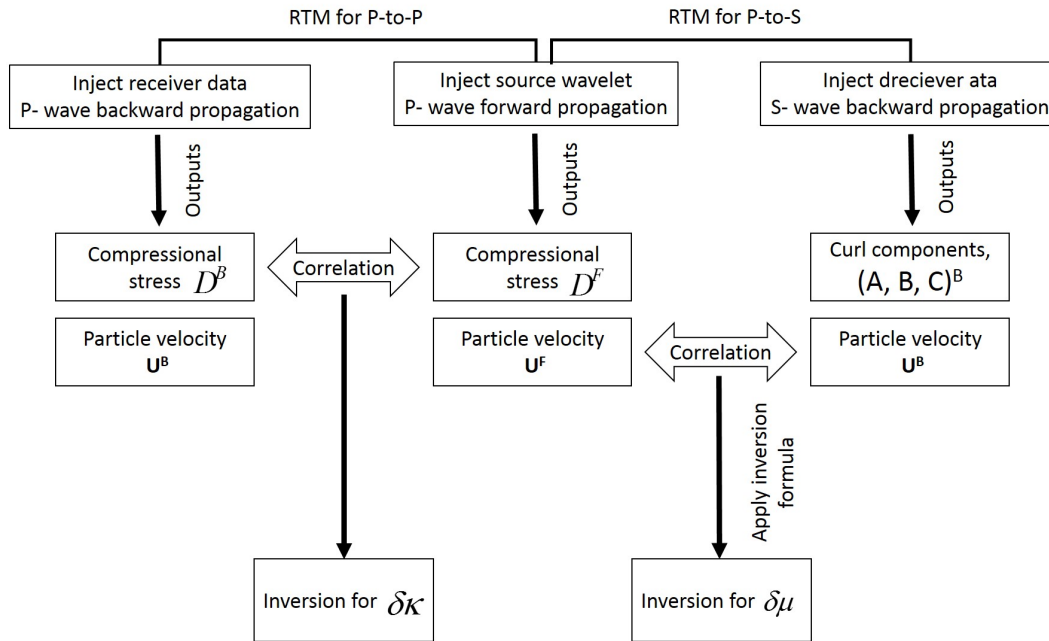


FIG. 5. The flow chart of the multicomponent RTM based on separation of P- and S- wave.

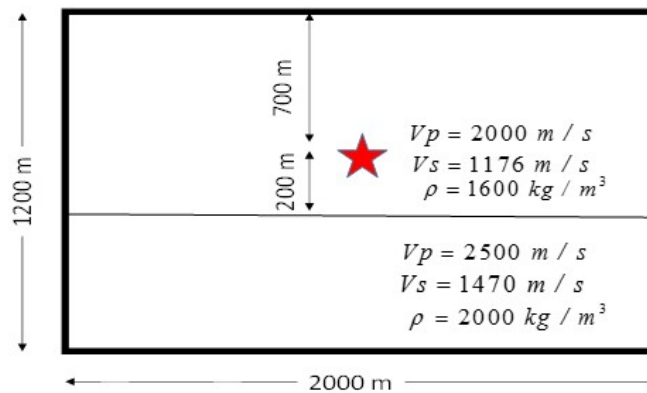


FIG. 6. The elastic two layer model with an explosion source buried at depth.

Figure (7), where the background color represents the inverted $\delta\hat{\kappa}(\mathbf{x}')$ and $\delta\hat{\mu}(\mathbf{x}')$. As seen, the continuity and intensity of $\delta\hat{\kappa}(\mathbf{x}')$ and $\delta\hat{\mu}(\mathbf{x}')$ are consistent with P- and S-wave types, where their strength can be correlated with reflectivity. The multiple P-to-P is observed to have stronger dilatation in Figure (7c) and weaker shearing values in Figure (7d) which is consistent with P-wave behavior.

NUMERICAL EXAMPLES

Blocky perturbation model

We demonstrate the performance of P-to-P and P-to-S wave separation using the flat-layered model in Figure (8a) with the perturbation in V_P and V_S . The density is set to be constant and equal to $2000 \frac{kg}{m^3}$. We generate 112 synthetic elastic shots from 50 m to 950 m of the model and evenly spaced at 8 m on the surface. Here, 251 receivers are evenly distributed at 4 m intervals on the surface. The P-wave point source uses a Ricker wavelet with a 25 Hz peak frequency, and the total recording time is 1.5 s. Figures (8b

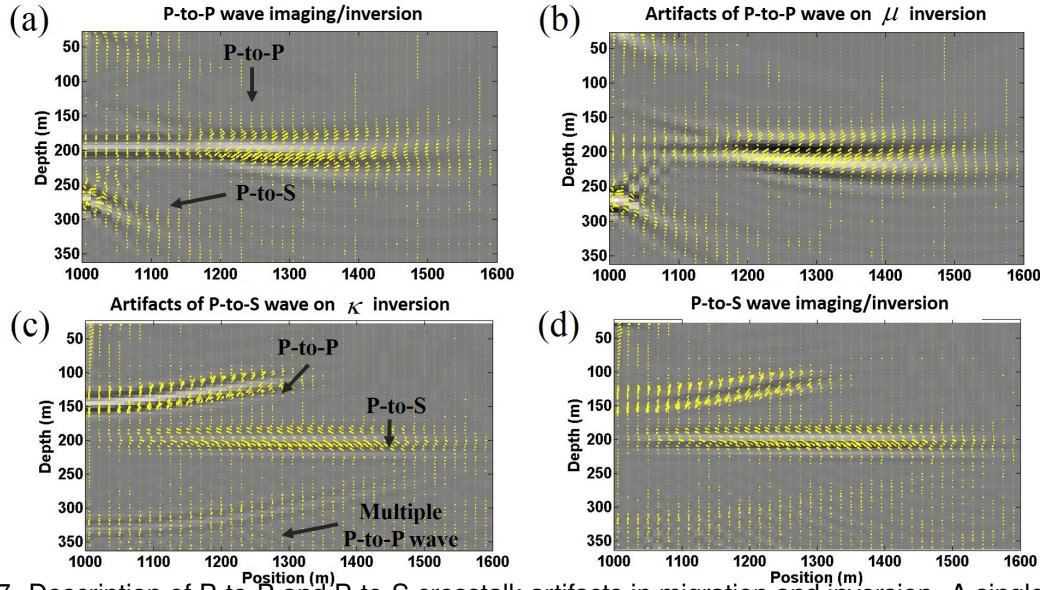


FIG. 7. Description of P-to-P and P-to-S crosstalk artifacts in migration and inversion. A single explosive source in elastic model shown in Figure (6) is modeled and migrated. The vectors illustrate the migration of displacement components and the background color are computed bulk modulus κ and shear modulus μ values based on inversion formulation in FWI method. a) Inversion from P-to-P data b) crosstalk of P-to-P data, c) crosstalk of P-to-S data, and d) inversion of shear modulus from P-to-S data.

and c) compare the P-to-P and P-to-S RTM images. As seen, the perturbations in V_P and V_S are consistent with the amplitude recovered in the inversion result of P-to-P and P-to-S data respectively. It is expected that the perturbation in V_S creates amplitude image in P-to-P images. This artifact arises from the inversion formula of equation 11. In numerical applications, because of smaller amplitude in the shorter angle of incident, after stacking the migrated shot records, the amplitude of this artifact is small with reversed polarity. The P-to-S image due to V_S has higher resolution as compared with the corresponding image in the P-to-P image due to the shorter wavelength of S-waves. As seen, the crosstalk noise of P- and S- waves in imaging create an additional artifact that affects the true amplitude images. Different types of migration can be applied in the inversion process. The accuracy of the method depends on the efficiency of true amplitude migration. It is expected that the approach of least square migration and deconvolution migration improves the efficiency of true amplitude migration and inversion. .

Marmousi Ocean Bottom Cable (OBC)

The Marmousi elastic model (Martin et al., 2006) is chosen because it is a marine environment, where the incident wave has initiated a P- wave in an acoustic environment, propagates the P- wave and S-wave below the water layer and the OBC receivers record both of P-wave and upgoing S-waves. The P- and S-wave velocity and density models are shown in Figure (9). Our objective is to compare the advantage of P-to-P and P-to-S wave imaging and inversion using wave separation for the areas with smooth lateral variation in elastic properties and the complex structure of the model. For this study, A total of 400 shots were simulated with a source interval of 20 m starting at 100 m from the left edge of the model. All of the sources are at a water depth of 10 m. A 17 Hz Ricker wavelet is

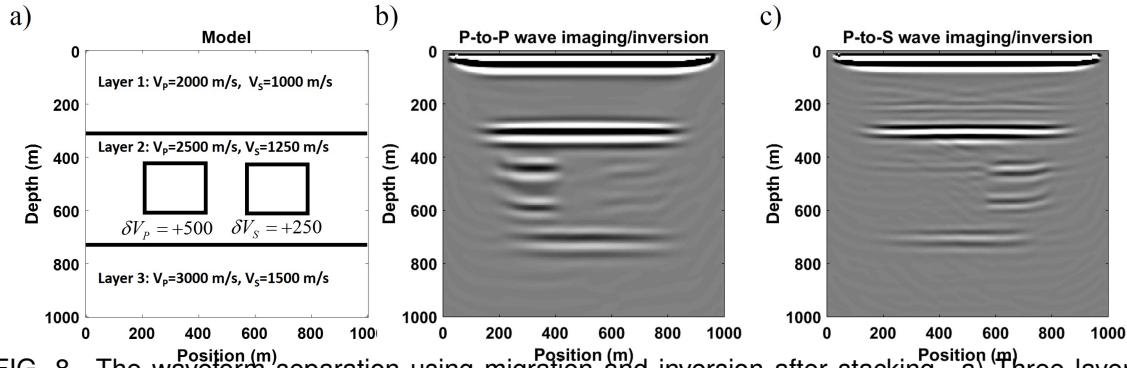


FIG. 8. The waveform separation using migration and inversion after stacking. a) Three layers model with perturbation in V_P and V_S . b) Inversion from P-to-P data, c) Inversion from the P-to-S data.

used as the source. The receivers are deployed on the ocean bottom at 500 m water depth with the maximum offset of 5000 m in split spread configuration and evenly spacing of 5 m. The total recording time is 5.0 s. A free-surface boundary condition was applied at the top to generate multiples.

The migration/inversion is performed by the same parameters of acquisition without performing any preprocessing steps for P- and S- waves separation and the multiples removal. General features of the model are reconstructed by both waves. The combination of the acquisition fold on the reflectors as a result of number of shots, offset range of source and receiver spread, their position and complexity of the structures such that the specular energy of reflected P- and S- waves with the AVO effects play the main role in quality of true amplitude P- and S-waves imaging/inversion results.

Figure (10) shows the P- and S- wave impedance from the simple portion of the Marmousi model, where the lateral variation of elastic properties are smooth. The result of P-to-P wave migration/inversion for this portion is compared with the inversion result obtained from the P-to-S waves. As seen, the S-wave provides more details about layer boundaries. The P-to-P wave is sensitive to the V_P and ρ anomalies as indicated by arrows. In addition, on the depth of 1050 m in the problem of P-to-P multiple is observed, while this problem is not observed in the result obtained from the P-to-S wave.

For the more complex structure of the model, we simulate 100 shot from 8000 m to 10000 m of the model with the same acquisition parameters used in Figure (10). The results are compared in Figure (11) where they show different sensitivity and amplitude continuity of the reflectors for a different portion of the structures. For example, the arrows show the strong contrast in V_P and ρ which have been recovered with P-to-P wave imaging/inversion. The problem of P- wave multiple is still present in b, while the P-to-S image does not show this problem.

As seen in Figures (2 and 4), collocation of P- and S- wave produce numerical crosstalk artifact in inversion result which creates inaccuracy to the inversion results if the fully elastic RTM was used. To quantify these errors in the imaging of Marmousi model, we estimate the applied the inversion equation 11 for μ from the P-to-P image (see Figure (12a)), and applied the inversion formula for κ from P-to-S image (see Figure (12b)). Comparison of the inversion results of μ and κ show the importance of P- and S- wave separation in practical imaging and inversion because with increasing the complexity of geological structure, the P-to-P and P-to-S- wave response can be migrated with different quality.

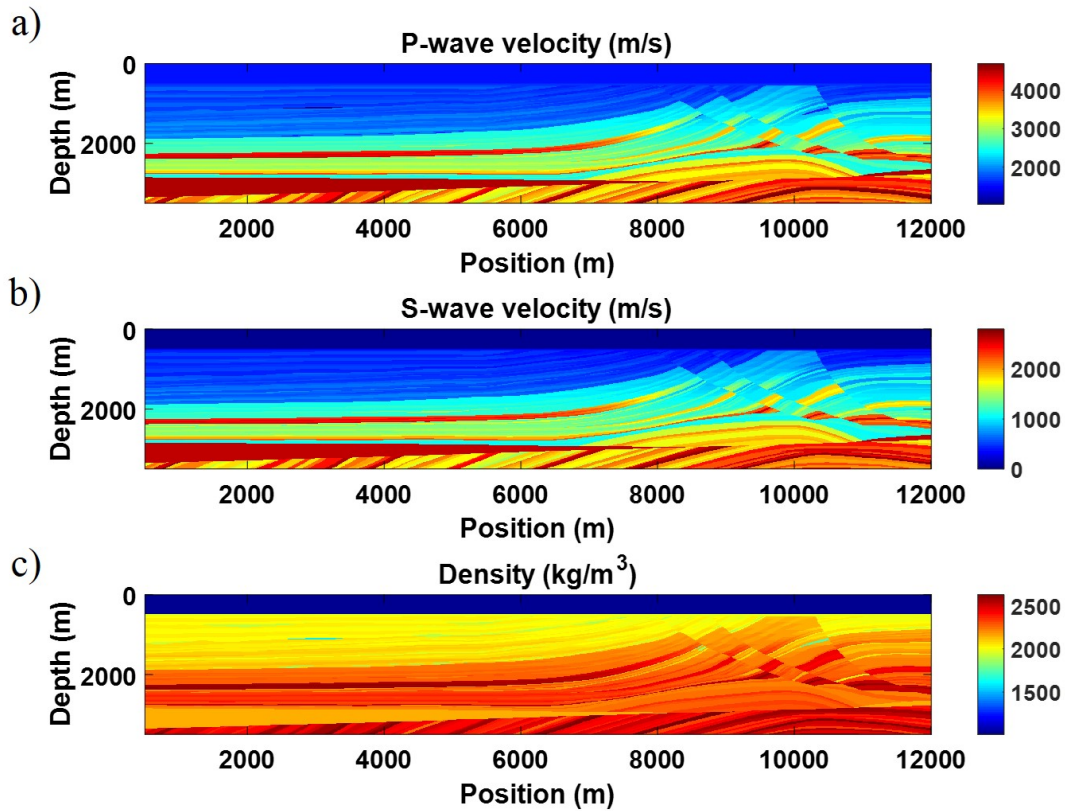


FIG. 9. Marmousi 2 elastic model. a) P-wave velocity, b) S-wave velocity and c) density.

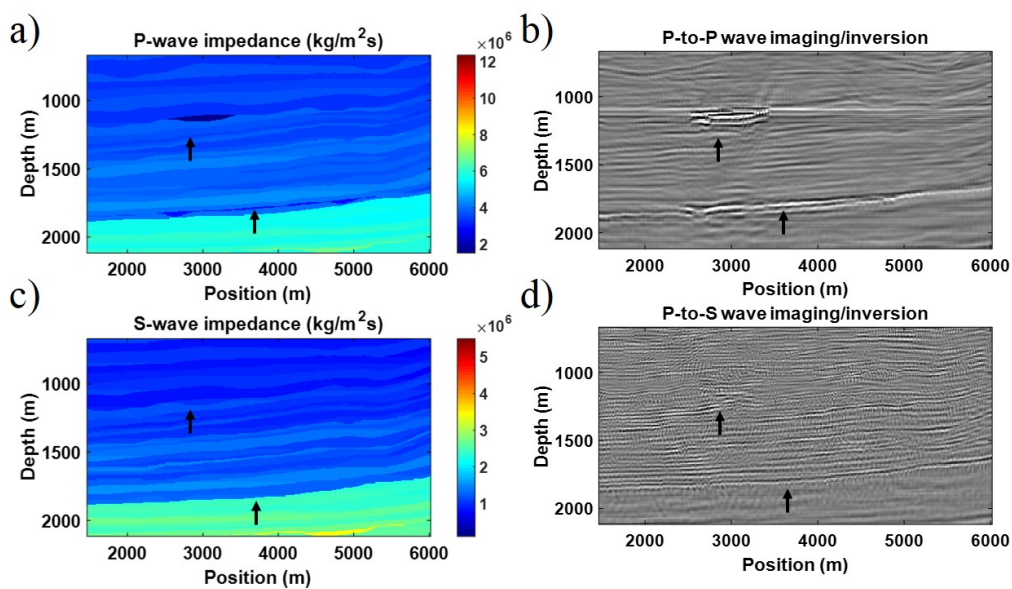


FIG. 10. Marmousi 2 elastic model migration and inversion in smooth lateral variation in elastic properties. a) P-wave impedance, b) inversion of κ from P-to-P data, c) S-wave impedance, d) inversion of mu from P-to-S data. The arrows indicate stronger anomalies in P-wave impedance when compared to S-wave impedance.

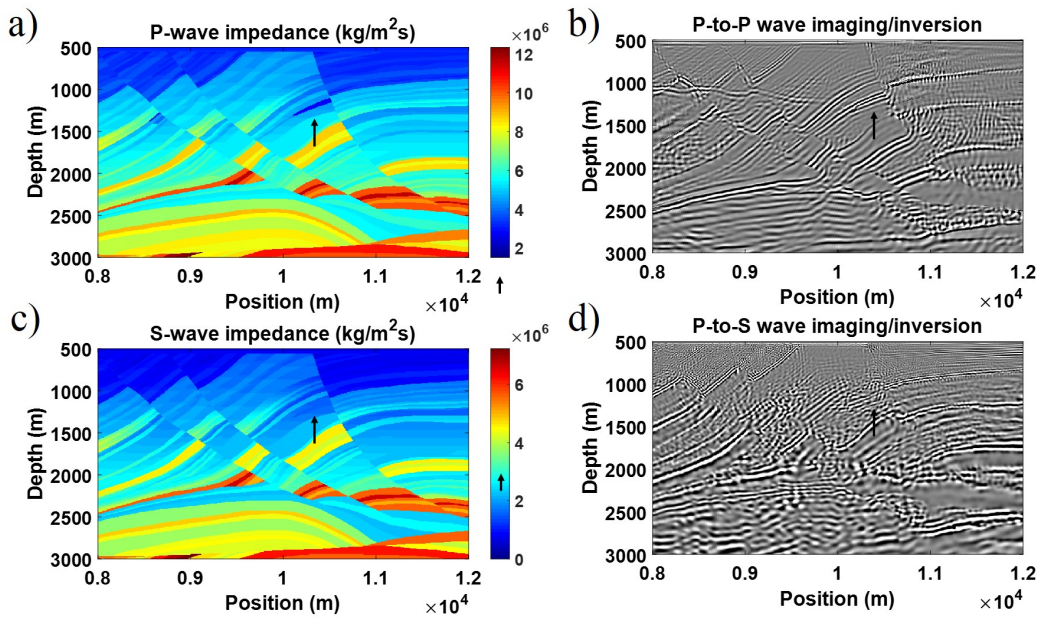


FIG. 11. Marmousi 2 elastic model migration and inversion in complex portion of the model. a) P-wave impedance, b) inversion of κ from P-to-P data, c) S-wave impedance, d) inversion of μ from P-to-S data. The arrows indicate stronger anomalies in P-wave impedance when compared to S-wave impedance.

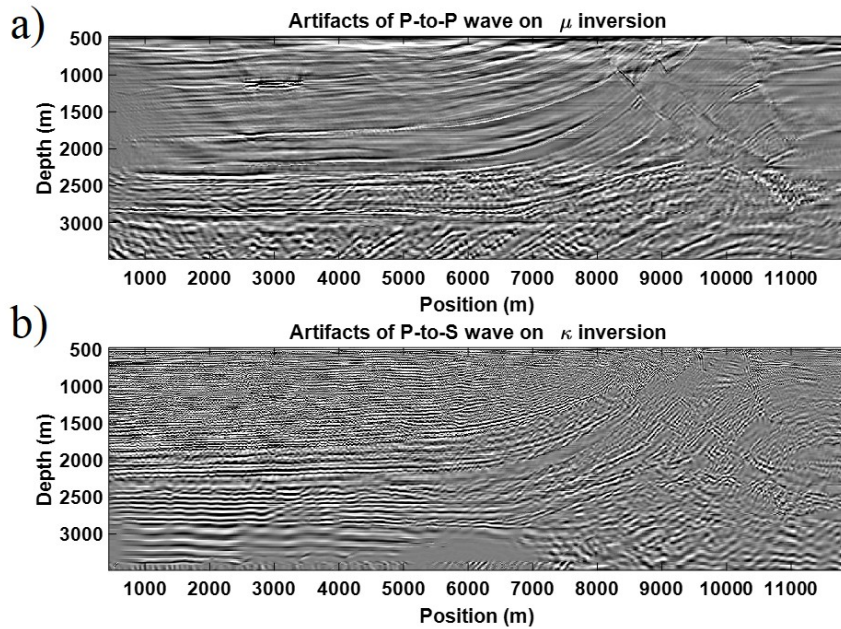


FIG. 12. Marmousi 2 elastic model crosstalk produced by a) P-to-P waves and b) P-to-S wave.

APPLICATION TO ANISOTROPIC MEDIUM

The presented approach is applicable to a general anisotropic medium, where the multiparameters are extracted by (Tarantola, 1988),

$$\begin{aligned}\delta\hat{\rho}(\mathbf{x}) &= \int dt \frac{\partial U_j^F}{\partial t} \frac{\partial U_j^B}{\partial t} \\ \delta\hat{c}^{ijkl}(\mathbf{x}) &= - \int dt \frac{\partial U_i^F}{\partial x_j} \frac{\partial U_k^B}{\partial x_l}.\end{aligned}\tag{17}$$

For a general anisotropic medium, the pseudo-pure qP wave propagation of Cheng and Kang (2014) can be implemented. Similarly, for the S- wave propagation, the pseudo pure mode qS of Cheng and Kang (2016) can be implemented in the algorithm. Therefore, the receiver backward propagation for P-to-P and P-to-S and SH-to-SH waves are solved with pseudo-pure qP and qSv and qSH modes respectively. Compared to full wave-equation, solution of the migration and inversion problem with the separated equation reduces the computation costs for 3D problems.

DISCUSSION

In the presented algorithm, the differences between both of traveltime and amplitude of P-to-P and P-to-S waves lead to separation of P- and S- waves. Consequently, the higher ratio of $\frac{V_P}{V_S}$ increase cancellation of the unwanted waveform during stacking of migrated shots which lead to an improved quality of wave separation. In this approach, to have efficient cancellation effects, the number of shot records is high compared to fully elastic RTM. The RTM has source forward propagation that is solved by acoustic approximation. We expect numerical artifacts due to multiples data because the imaging condition is designed for primary P-to-P and P-to-S waves. Hence, additional preprocessing are helpful to remove the multiples and other mode converted waves such as S-to-P. Compared to full elastic RTM, the presented algorithm does not fully compensate the true amplitude loss due to mode conversion. In addition, the FWI method is known to be an iterative optimization problem with the objective of minimizing the data residuals and updating model parameters. In this study, the inversion result of one step is presented for reflected waves. The approach is applicable to iterative schemes.

CONCLUSIONS

We studied the gradient functions of the full waveform inversion in the context of reflection problem. We showed that the gradient functions have the problem of crosstalk artifacts of P- and S- wave collocation if solved with Reverse Time Migration (RTM) with full wave equation. To reduce the errors associated with P- and S- wave collocation, we developed a multicomponent RTM algorithm for separation of P- and S- wave in the image domain. The multicomponent algorithm is based on decoupled P- and S- wave propagation and the imaging condition of gradient functions in FWI. We present the numerical experiment to quantify the uncertainty of P- and S- wave separation in simple and complex structures in Marmousi elastic model. The limitation in the acquisition and the difference in

amplitude radiation response of P- and S-wave at the specular angle can lead to two images with a different illumination of the reflector response that may not be identified if full wave equations are used. The approach is computational faster as compared to the use of full wave equation. The method is applicable to solve the problems associated with the various type of anisotropy for imaging problems of seismic and microseismic data in surface and downhole acquisition.

CONCLUSIONS

The authors acknowledge the support from sponsors of CREWES and NSERC (Natural Science and Engineering Research Council of Canada) through the grant CRDPJ 461179-13.

REFERENCES

- Aki, K., and Richards, P. G., 2002, *Quantitative Seismology*: University Science Books, 2nd edn.
- Beylkin, G., 1985, Imaging of discontinuities in the inverse scattering problem by inversion of a causal generalized radon transform: *J. Math. Phys.*, **26**, 99–108.
- Beylkin, G., and Burridge, R., 1990, Linearized inverse scattering problems in acoustics and elasticity: *Wave motion*, **12**, 15–52.
- Bleistein, N., 1979, Velocity inversion procedure for acoustic waves: *Geophysics*, **44**, 1077–1087.
- Chen, K., 2014, Finite-difference simulation of elastic wave with separation in pure p- and s-modes: *Journal of Computational Methods in Physics*, **2014**, 1–14.
- Cheng, J., and Kang, W., 2014, Simulating propagation of separated wave modes in general anisotropic media, part i: qp-wave propagators: *Geophysics*, **79**, C1–C18.
- Cheng, J., and Kang, W., 2016, Simulating propagation of separated wave modes in general anisotropic media, part ii: qs-wave propagators: *Geophysics*, **81**, C39–C52.
- Dankbaar, J. W. M., 1985, Separation of p- and s-waves: *Geophysical Prospecting*, **33**, 970–986.
- Dellinger, J., and Etgen, J., 1990, Wave-field separation in two-dimensional anisotropic media: *Geophysics*, **55**, 914–919.
- Martin, G. S., Wiley, R., and Marfurt, K. J., 2006, Marmousi2: An elastic upgrade for marmousi: *The Leading Edge*, **25**, 156–166.
- Schuster, G., 2015, *Sesimic inversion*: Society of Exploration Geophysics.
- Sun, R., and McMechan, G. A., 1994, Marmousi2: An elastic upgrade for marmousi: *Geophysics*, **66**, 1519–1527.
- Tarantola, A., 1984, Inversion of seismic reflection data in the acoustic approximation: *Geophysics*, **49**, 1259–1266.
- Tarantola, A., 1986, A strategy for nonlinear elastic inversion of seismic reflection data: *Geophysics*, **51**, 1893–1903.
- Tarantola, A., 1988, Theoretical background for the inversion of seismic waveforms including elasticity and attenuation: *Pure and Applied Geophysics*, **128**, 365–399.
- Virieux, J., 1986, P-sv wave propagation in heterogeneous media, velocity-stress finite difference method: *Geophysics*, **51**, 889–901.

Zhou, M., 2005, A well-posed pml absorbing boundary condition for 2d acoustic wave equation: University of Utah, **72**, R109–R114.